

# Bifurcation and Chaos in Size-Dependent NEMS Considering Surface Energy Effect and Intermolecular Interactions

S. Rahmanian, Sh. Hosseini-Hashemi \*

*School of Mechanics Engineering, Iran University of Science and Technology, Narmak, Tehran, Iran*

Received 23 February 2019; accepted 17 April 2019

## ABSTRACT

The impetus of this study is to investigate the chaotic behavior of a size-dependent nano-beam with double-sided electrostatic actuation, incorporating surface energy effect and intermolecular interactions. The geometrically nonlinear beam model is based on Euler-Bernoulli beam assumption. The influence of the small-scale and the surface energy effect are modeled by implementing the consistent couple stress theory proposed by Hadjesfandiari and Dargush together with Gurtin-Murdoch elasticity theory. The governing differential equation of motion is derived using Hamilton's principle and discretized to a set of nonlinear ODE through Galerkin's method. Nonlinearities stemmed from different sources such as mid-plane stretching, electrostatic and interatomic forces lead to an intensive nonlinear dynamics in nano-electro-mechanical devices so that the systems exhibit rich dynamic behavior such as periodic and chaotic motions. Poincaré portrait is utilized in order to present the system dynamic response in discrete state-space. Bifurcation analysis has been performed with a change in the magnitude of AC voltage corresponding to the various values of DC voltage and excitation frequency. Then, we compare some ranges of AC voltage amplitude, in which the system response becomes stable for these cases. Fast Fourier transformation is also carried out to analyze the frequency content of the system response.

© 2019 IAU, Arak Branch. All rights reserved.

**Keywords :** Size-dependent NEMS; Bifurcation; Chaos; Poincaré portrait; FFT analysis.

## 1 INTRODUCTION

BY advances in the nanotechnology, nano-electro-mechanical systems (NEMS) have become one of the most commonly used components in constructing sensors and actuators. Because of their exemplary advantages such as small size, low cost, remarkable reliability, and higher precision, NEMS devices are being utilized in wide variety of applications such as capacitive sensors, resonators, filters, mass and force detection, random accessing memories and atomic force microscopes. Nonlinearities in NEMS resonators generally arise from two different sources:

---

\*Corresponding author. Tel.: +98 2177242912; Fax: +98 2177240488.  
E-mail address: [shh@iust.ac.ir](mailto:shh@iust.ac.ir) (Sh. Hosseini-Hashemi).

relatively large structural deformations, and displacement-dependent forces including electrostatic excitations and interatomic interactions (van der Waals and Casimir forces). When a beam is oscillating between two parallel electrodes, chaos may occur in the response of the system due to the development of a Duffing-type oscillator. Chaos is a type of nonlinear motion known as an undesirable phenomenon in the dynamic response of many systems. The unpredictable nature of the system's behavior re-proves the importance of studying chaotic dynamics in modeling a nanobeam-based actuator.

In the recent years, a great deal of research has been carried out in the literature on the chaotic behavior of NEMS/MEMS resonators. F. N. Mayoof and M. A. Hawwa [1] studied the chaotic behavior of a curved carbon nanotube under harmonic excitation. They analyzed the dynamic response of the resonator in the context of the bifurcation theory. T.D. Amorim et al [2] analyzed the chaotic behavior of MEMS fixed-fixed beam resonators using an improved 1-DOF model. They found chaotic regime in a small region of the parameter space, close to the dynamic pull-in. Lyapunov exponent and bifurcation diagrams were calculated to fully characterize the system response. S. Sabarathinam et al [3] investigated the chaotic dynamics of a system of generalized Duffing-type MEMS resonator through implementing an analog electronic circuit. W. Hu et al. [4] investigated the effects of elastic boundary restraints on the chaotic properties of a single-walled carbon nanotube. Their results indicate that the relative bending stiffness coefficient and the absolute bending stiffness coefficients at both ends of the carbon nanotube are two important factors that affect the chaotic region of the system, which provides guidance on the design and manufacture of precise micro/nano mechanical systems. Bienstman et al. [5] developed an autonomous impact resonator by taking advantage of the pull-in instability in an electrostatic microbeam resonator without a separate control circuit. The frequent impact, which caused chaos, was produced by driving the electrode at a voltage higher than the pull-in voltage. They also reported experimental evidence of period doubling behavior. Luo and Wang [6, 7] studied the resonant conditions and chaotic motion of a simplified time varying capacitor. They reported chaotic response in a certain frequency band of the MEMS device. DeMartini et al. [8] used a version of the Mathieu equation in order to model the governing motion's equation of MEMS oscillators and utilized the well-known Melnikov's method to obtain an inequality that predicts the region of the parameter space where chaos exists. Theoretical analysis and experimental results on the dynamic behavior of a bistable MEMS resonator were presented by Wang et al. [9]. They also demonstrated the existence of a strange attractor and chaos in the MEMS devices. Zhang et al. [10] studied the nonlinear dynamics and chaotic motion of the resonators under random excitation both analytically and numerically. The essential conditions for occurrence of chaos in the stochastic systems are derived based on the random Melnikov approach. Aghababa [11] investigated the conditions of chaos existence in a non-autonomous fractional-order MEMS resonator using the maximum Lyapunov exponent criterion. Li et al. [12] presented analytical proof on the existence of chaos in a generalized Duffing-type oscillator with fractional order deflection. They proposed an analytical formulation for the two homoclinic orbits and utilized the Melnikov's technique to derive the criteria for transverse intersection of the stable and unstable manifolds. E.M. Miandoab et al. [13] categorized the resonator dynamics to four physical situations based on the potential function and phase portrait of the corresponding unperturbed system. They also showed that the homoclinic bifurcation occurs when the system steady state velocity or amplitude reaches the homoclinic orbit maximum speed or amplitude. Seleim et al. [14] studied the bifurcation and chaos of a close-loop electrostatic MEMS resonator and determined an optimal region for long-stroke actuating. J. Han et al. [15] presented the design considerations on large amplitude vibration of a doubly clamped microresonator with two symmetrically located electrodes. According to the energy of potential barrier/well or the homoclinic/heteroclinic orbits, large amplitude vibration and dynamic pull-in phenomenon were explained quantitatively, and the corresponding parameter regions were established. Haghighi and Markazi [16], also used the Melnikov's technique for chaos prediction in the resonators and then they stabilized the periodic orbit embedded in the system response by applying the robust adaptive fuzzy control strategy. Besides, fuzzy sliding mode control [17], second-order fast terminal sliding mode control [18], state dependent Riccati equation control and optimal linear feedback control strategies [19, 20] were proved to be executable to the function of this type of resonator. F. Tajaddodianfar et al. [21] investigated the chaotic vibration of a bistable resonator comprised of a double clamped initially curved microbeam resonator. They studied the effects of various parameters including the arch curvature, the actuation parameters and the quality factor of the resonator. Ni et al. [22] scrutinized the nonlinear dynamics of an electrically-driven suspended silicon nanowire, and demonstrated that multi-stability leads to chaotic regime. W. Hu et al. [23] addressed chaos phenomenon in an embedded single-walled carbon nanotube, and presented analytical condition and numerical results of chaotic vibration of CNT. Coluci et al. [24] observed the existence of chaotic and regular motions for a given total energy in coupled oscillators based on multi-walled carbon nanotubes. The nonlinear vibrations of a single-walled CNT and a double-walled CNT under harmonic excitation near their primary resonance have been investigated by Mayoof and Hawwa [1, 25, 26]. Hawwa also rendered some numerical results related to chaos and bifurcation in the CNT. Joshi et al. [27] observed chaos in a single-walled

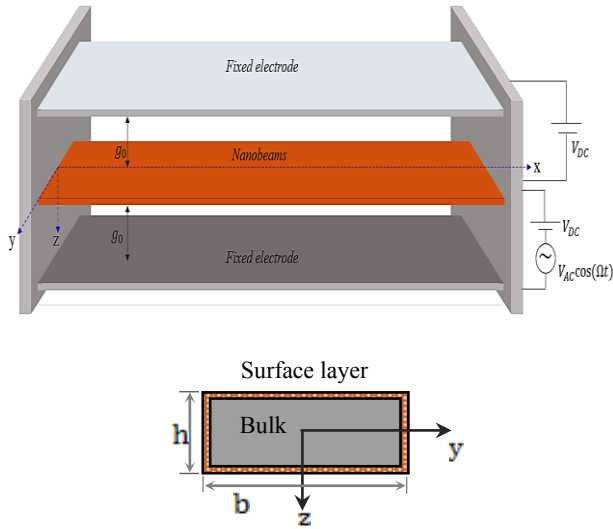
carbon nanotube and obtained some qualitative properties for the nonlinear dynamics of the carbon nanotube. Chaos has also been detected in tapping mode AFM through simulations and experiments [28-30]. An AFM probe is composed of a microcantilever beam and a tip at its free end in close vicinity to the surface of a specimen. Ashhab et al. [28] reported chaotic motion when the AFM probe is driven near its natural frequency to tap the sample surface. They modeled the beam-tip-sample interaction accounting for the damping and forcing. They found a homoclinic orbit and used analytical Melnikov's technique to find how the stable and unstable manifolds intersect in the presence of small perturbations produce chaos. J. M. Balthazar et al. [31] studied the nonlinear dynamics of a microcantilever probe in the presence of van der Waal forces. They proposed two control strategies in order to force the probe to avoid undesirable behavior such as chaotic motion. They also investigated the effect of parametric errors on the robustness of each control methodologies. The existence of chaos in AFM has also been reported via experimental studies where it was observed and characterized using fractal and correlation dimensions, Lyapunov exponents, and noise iteration calculations [32, 33]. Numerous investigations have been conducted on nonlinear response of MEMS/NEMS devices subjected to electrostatic actuating. Among many others, W. Lin and Y. Zhao [34] examined the nonlinear behavior of nanoscale electrostatic actuators with Casimir force. One degree of freedom mass-spring model is adopted and the bifurcation characteristics of the actuators are obtained. Abdel-Rahman and Nayfeh [35] investigated secondary resonances of electrically actuated resonant microsensors analytically using the multiple scales method. Nonlinear dynamics of an electrostatically actuated carbon nanotube (CNT) resonator are studied by Ouakad and Younis [36]. Shooting method is utilized to study the primary and secondary resonances [37, 38]. A. Rezaei Kivi et al. [39] presented a bifurcation analysis of an electrostatically actuated nano-beam based on modified couple stress theory. They evaluated the system static and dynamic pull-in behaviors, phase space characteristics and nonlinear frequency-response behavior of a NEMS device. Their results revealed that, for some values of DC voltage load, homoclinic orbit extends in the phase space diagram and it starts shrinking as the parameter approaches pull-in threshold. X. Chen et al. [40] investigated the dynamic behavior of a micro-resonator under various levels of Alternating Current (AC) voltage, without a biased Direct Current (DC) voltage. Their results revealed that, damping and boundary conditions remarkably affect the system dynamic behavior and the design diagrams of the system. A. Nikpourian et al. [41] studied the size-dependent static and dynamic behavior of a fully clamped microbeam under electrostatic and piezoelectric actuations. They showed that the piezoelectric voltage can effectively modify the flexural rigidity of the system which in turn affects the pull-in instability regime. S.M. Pourkiaee [42] investigated the parametric resonances of an electrically actuated piezoelectric nanobeam resonator considering surface effects and van der Waals forces. The influence of piezoelectric voltage, surface effects and interatomic forces are investigated on the natural frequencies, static equilibrium, pull-in voltage, and principle parametric resonance of the nanoresonator. Hajnayeb et al. [43, 44] investigated in detail the stability and the nonlinear oscillations of single-walled and double-walled CNTs under electrostatic actuation. Primary and secondary resonances and bifurcation points associated with different values of DC and AC voltages were studied based on the method of multiple-scale.

In the majority of the previous work mentioned in the literature, a lumped-mass model has been used to study the chaos phenomenon in nano/micro-electro-mechanical systems. This paper targets to comprehensively investigate the chaotic behavior of a clamped-clamped nano-beam oscillating between two parallel electrodes. Since the surface to volume ratio is significant in nanoscale structures, surface energy effect is considered based on the surface elasticity theory proposed by Gurtin and Murdoch. Also, a consistent size-dependent continuum theory is utilized in order to model the small-scale effect. Both the van der Waals and the Casimir forces are considered as intermolecular interactions between the fixed and movable electrodes. The dynamical behaviors are numerically identified in discrete state space, based on the Poincaré portraits. The effect of electrostatic force parameters including DC and AC voltages and the excitation frequency on the system dynamic response is studied. Bifurcation diagrams are obtained by sweeping the AC voltage amplitude for different values of DC voltage and frequency. The main purpose of the present work is to capture some ranges of the bifurcation parameter of the NEMS system in presence of all nanosized structure effects, in which the periodic orbit embedded in the system response becomes stable. Fast Fourier Transformation (FFT) is also carried out to present the NEMS dynamic response in frequency domain.

## 2 MATHEMATICAL FORMULATION

Fig. 1 depicts a doubly clamped nanobeam under electrostatic actuation. The movable nanobeam is of length  $L$ , width  $b$ , and thickness  $h$  and is surrounded by a surface layer. Two electrodes are placed on top and underneath of the nanobeam. Initial gap between the nanobeam and the electrodes is  $g_0$ , and the applied electrostatic voltages

through the lower and upper electrodes are denoted by  $V_l$  and  $V_u$ , respectively. The applied voltage via the lower electrode is assumed to be a combination of a DC bias voltage,  $V_{DC}$ , and an AC voltage with amplitude  $V_{AC}$  and frequency  $\Omega$ , and the voltage applied through the upper electrode is a pure DC load, equal to the DC component of the lower electrode. As illustrated in Fig. 1, the  $xyz$  inertial coordinate system passes through the neutral axis of the undeformed beam and is located at the left clamped end of the nanobeam. The horizontal and vertical displacements of any material point located on the centroidal axis of the beam in  $x$  and  $z$ -directions are represented by  $u(x;t)$  and  $w(x;t)$ , respectively.



**Fig.1** Schematic diagram of a clamped–clamped nanobeam with double-sided electrostatic actuation.

The distributed interatomic forces induce an attractive force between the movable electrode and the two stationary electrodes. Two interaction regimes consist of van der Waals and Casimir forces can be considered. The equation for the former is:

$$F_{vdw} = \frac{A_h b}{6\pi} \left( \frac{1}{(g_0 - w(x,t))^3} - \frac{1}{(g_0 + w(x,t))^3} \right) \tag{1}$$

where  $A_h$  is the Hamaker constant with values in the range of  $[0.4-4] \times 10^{-19} J$  [45]. In addition, the formula for the latter is given by

$$F_{cas} = \frac{\pi^2 \hbar c b}{240} \left( \frac{1}{(g_0 - w(x,t))^4} - \frac{1}{(g_0 + w(x,t))^4} \right) \tag{2}$$

where  $\hbar = 1.055 \times 10^{-34} J$  denotes the Planck's constant divided by  $2\pi$ , and  $c = 2.998 \times 10^8 m/s$  is the speed of light [46]. The distributed electrostatic force can be written as:

$$F_{elec} = \frac{\epsilon_0 b V_l^2}{2(g_0 - w(x,t))^2} \left( 1 + 0.65 \frac{g_0 - w(x,t)}{b} \right) - \frac{\epsilon_0 b V_u^2}{2(g_0 + w(x,t))^2} \left( 1 + 0.65 \frac{g_0 + w(x,t)}{b} \right) \tag{3}$$

In expressing Eq. (3), the fact has been taken into account that the geometry is far from infinite plate capacitors, where the fringing field effect is negligible [47, 48]. Therefore, a first-order fringing field correction is included through the second terms in the parentheses.

## 2.1 Bulk energy

According to experimental results [49, 50], the mechanical behavior of materials in small scales is different from their behavior at macro-scales. In fact, classical continuum mechanics of solids is based on the assumption that matter is continuously distributed throughout the solid. Thus, the classical continuum theories governing the mechanical behavior of macro-materials often fail to predict the characteristics of the nano/micro-structures. In the present work, the consistent couple stress theory (CCST) proposed by Hadjesfandiari and Dargush is applied to take into account the effect of size and discrete nature of the nanobeam keeping the continuity assumption. Based on CCST, The strain energy density stored in elastic bulk materials with infinitesimal deformations occupying volume  $V$  is given by [51]:

$$U_B = \frac{1}{2} \int_V (\sigma_{ji} e_{ij} + \mu_{ji} \kappa_{ij}) dV \quad (4)$$

where  $\sigma_{ji}$ ,  $e_{ij}$ ,  $\mu_{ji}$  and  $\kappa_{ij}$  denote, respectively, the non-symmetric force-stress tensor, strain tensor, skew-symmetric couple-stress tensor and skew-symmetric mean curvature tensor, which are obtained as follows:

$$\begin{aligned} e_{ij} &= \frac{1}{2}(u_{i,j} + u_{j,i}), \quad \omega_{ij} = \frac{1}{2}(u_{i,j} - u_{j,i}), \quad \omega_i = \frac{1}{2} \varepsilon_{ijk} \omega_{kj}, \quad \kappa_{ij} = \frac{1}{2}(\omega_{i,j} - \omega_{j,i}), \\ \sigma_{ji} &= \lambda e_{kk} \delta_{ij} + 2\mu e_{ij} + 2\mu l^2 \nabla^2 \omega_{ji}, \quad \mu_{ji} = -8\mu l^2 \kappa_{ji} \end{aligned} \quad (5)$$

In above equations,  $\omega_{ij}$  represents the skew-symmetric rotation tensor and  $\omega_i$  defines the corresponding dual vector.  $\varepsilon_{ijk}$  denotes the permutation or Levi-Civita symbol,  $\lambda$  and  $\mu$  represent Lamé's constant, and  $l$  is the materials' length-scale parameter.

For the Euler-Bernoulli beam, the displacement field for each arbitrary material point can be expressed as:

$$U_x(x, z; t) = u(x; t) - z \frac{\partial w(x; t)}{\partial x}, \quad U_y(x, z; t) = 0, \quad U_z(x, z; t) = w(x; t) \quad (6)$$

Assuming low slope for the beam after transformation and using the von-Karman nonlinearity for midplane stretching, the only non-zero component of the strain tensor can be expressed as:

$$e_{xx} = \frac{\partial U_x}{\partial x} + \frac{1}{2} \left( \frac{\partial U_z}{\partial x} \right)^2 = \frac{\partial u(x, t)}{\partial x} - z \frac{\partial^2 w(x, t)}{\partial x^2} + \frac{1}{2} \left( \frac{\partial w(x, t)}{\partial x} \right)^2 \quad (7)$$

For the case of a slender beam with large aspect ratio, the Poisson effect can be ignored to simplify the formulation of the nanobeam. Accordingly, the force-stress component in  $x$ -direction is presented in Eq. (8) and the rest of the components are assumed to be zero.

$$\sigma_{xx} = E e_{xx} = E \left[ \frac{\partial u}{\partial x} - z \frac{\partial^2 w}{\partial x^2} + \frac{1}{2} \left( \frac{\partial w}{\partial x} \right)^2 \right] \quad (8)$$

where  $E$  is Young's modulus of the bulk material. For a wide beam ( $b > 5h$ ),  $E$  is replaced by the effective modulus  $E/(1-\nu^2)$  [52]. Using Eq. (5), non-zero components of the rotation tensor, mean curvature tensor and couple-stress tensor are respectively expressed as:

$$\omega_{xz} = -\omega_{zx} = -\frac{\partial w}{\partial x}, \quad \kappa_{xy} = -\kappa_{yx} = \frac{1}{2} \frac{\partial^2 w}{\partial x^2}, \quad \mu_{xy} = -\mu_{yx} = 4\mu l^2 \frac{\partial^2 w}{\partial x^2} \quad (9)$$

Substituting Eqs. (7)-(9) into Eq. (13), the strain energy stored in the bulk material of the nanobeam can be obtained as follows:

$$U_B = \frac{EA}{2} \int_0^L \left( \frac{\partial u}{\partial x} + \frac{1}{2} \left( \frac{\partial w}{\partial x} \right)^2 \right)^2 dx + \frac{(EI + 4\mu AI^2)}{2} \int_0^L \left( \frac{\partial^2 w}{\partial x^2} \right)^2 dx \quad (10)$$

where  $I$  denotes the second moment of area of the cross section of the nanobeam, and  $A$  represents the area of the beam cross section.

## 2.2 Surface energy

The intensive decrease in size of the nano-actuators leads to significant surface to volume ratio, and therefore, the surplus energy of the beam's surface will contribute to its total strain energy. Gurtin and Murdoch [53, 54] adopted the classical continuum theory and proposed a formulation for surface elasticity model, where the surface of solids can be considered as a two-dimensional elastic membrane with different material constants, perfectly bonded to the bulk material without slipping. Based on the surface elasticity theory, the non-zero components of the surface stresses are

$$\begin{aligned} \tau_{xx} &= \tau_0 + E^s e_{xx} \\ \tau_{nx} &= \tau_0 n_z \frac{\partial w}{\partial x} \end{aligned} \quad (11)$$

where  $\tau_0$  and  $E^s$  are surface residual stress and surface elastic modulus, respectively.  $n_z$  is the  $z$ -component of the unit outward normal vector  $n$  to the beam surface. The contribution of the surface energy to the system total strain energy is given by [55]:

$$U_S = \frac{1}{2} \oint_{\partial A} \left( \tau_{xx} e_{xx} + \tau_{nx} n_z \frac{\partial w}{\partial x} \right) dS \quad (12)$$

where  $\partial A$  is the undeformed surface area of the beam. For a differential element of the surface layer,  $dS = d\bar{A} dx$ , where  $d\bar{A}$  is the differential perimeter element. Introducing Eqs. (7) and (11) into Eq. (12), the surface energy can be found in the form of:

$$U_S = \frac{1}{2} \oint_{\partial A} \left( \tau_0 \left( \frac{\partial u}{\partial x} - z \frac{\partial^2 w}{\partial x^2} + \frac{1}{2} \left( \frac{\partial w}{\partial x} \right)^2 \right) + E^s \left( \frac{\partial u}{\partial x} - z \frac{\partial^2 w}{\partial x^2} + \frac{1}{2} \left( \frac{\partial w}{\partial x} \right)^2 \right)^2 + \tau_0 n_z^2 \left( \frac{\partial w}{\partial x} \right)^2 \right) dS \quad (13)$$

It is worth mentioning that  $\tau_{xx}$  and  $\tau_{nx}$  are distributed along the entire perimeter of cross section. Neglecting the higher order terms, the surface elastic energy yields to:

$$\begin{aligned} U_S &= \frac{\tau_0 A^s}{2} \int_0^L \left( \frac{\partial u}{\partial x} + \frac{1}{2} \left( \frac{\partial w}{\partial x} \right)^2 \right) dx - \frac{\tau_0 P_A}{2} \int_0^L \left( \frac{\partial^2 w}{\partial x^2} \right) dx + \frac{E^s A^s}{2} \int_0^L \left( \frac{\partial u}{\partial x} + \frac{1}{2} \left( \frac{\partial w}{\partial x} \right)^2 \right)^2 dx + \\ &\frac{E^s I^s}{2} \int_0^L \left( \frac{\partial^2 w}{\partial x^2} \right)^2 dx + \frac{\tau_0 S_P}{2} \int_0^L \left( \frac{\partial w}{\partial x} \right)^2 dx \end{aligned} \quad (14)$$

where  $P_A$  and  $I^s$  are the first and second moments of the surface area, respectively. Note that for the case of symmetric cross section about  $y$ -axis,  $P_A = 0$ .  $A^s$  is the perimeter of the beam cross section. These cross-sectional properties are

$$P_A = \oint_{\partial \bar{A}} z d\bar{A}, \quad I^s = \oint_{\partial \bar{A}} z^2 d\bar{A}, \quad A^s = \oint_{\partial \bar{A}} d\bar{A}, \quad S_p = \oint_{\partial \bar{A}} n_z^2 d\bar{A} \quad (15)$$

### 2.3 Equation of motion

In this section, the differential equation of motion governing the NEMS behavior is derived by means of the energy method. The total strain energy of the nanobeam that is composed of the strain energies of the bulk material and of the surface layer can be found in the form of:

$$U = U_B + U_S \quad (16)$$

Neglecting the rotary inertia effect, the total kinetic energy of the nanobeam which consists of the kinetic energies of the bulk and of the surface layer is expressed as:

$$\begin{aligned} T &= \frac{1}{2} \int_V \rho \left( \left( \frac{\partial U_x}{\partial t} \right)^2 + \left( \frac{\partial U_z}{\partial t} \right)^2 \right) dV + \frac{1}{2} \oint_{\partial \bar{A}} \rho^s \left( \left( \frac{\partial U_x}{\partial t} \right)^2 + \left( \frac{\partial U_z}{\partial t} \right)^2 \right) dS \\ &= \frac{(\rho A + \rho^s A^s)}{2} \int_0^L \left( \left( \frac{\partial u}{\partial t} \right)^2 + \left( \frac{\partial w}{\partial t} \right)^2 \right) dx \end{aligned} \quad (17)$$

where  $\rho$  and  $\rho^s$  are the mass density of the bulk and surface layer, respectively. The external work done by the electrostatic, van der Waals and Casimir forces is equal to:

$$W_{nc} = \int_0^L \int_0^w (F_{elec} + \{F_{vdW} \text{ or } F_{cas}\}) dw dx \quad (18)$$

Relying on the fact that the variation of the integral of the extended Hamiltonian over the time interval  $[t_1, t_2]$  vanishes, namely,  $\delta \int_{t_1}^{t_2} (T - U + W_{nc}) dt = 0$ , the governing motion's equation and the associated boundary conditions are obtained as:

$$\begin{aligned} (EI)_{eq} \frac{\partial^4 w(x,t)}{\partial x^4} + (\rho A)_{eq} \frac{\partial^2 w(x,t)}{\partial t^2} - \left[ F_s + \frac{(EA)_{eq}}{2L} \int_0^L \left( \frac{\partial w}{\partial x} \right)^2 dx \right] \frac{\partial^2 w(x,t)}{\partial x^2} + 4\mu A l^2 \frac{\partial^4 w(x,t)}{\partial x^4} = \\ \frac{\varepsilon_0 b}{2} \left( V_l^2 \left( \frac{1}{(g_0 - w)^2} + \frac{0.65}{b} \frac{1}{g_0 - w} \right) - V_u^2 \left( \frac{1}{(g_0 + w)^2} + \frac{0.65}{b} \frac{1}{g_0 + w} \right) \right) + \\ \left\{ \frac{A_h b}{6\pi} \left( \frac{1}{(g_0 - w)^3} - \frac{1}{(g_0 + w)^3} \right) \text{ or } \frac{\pi^2 \hbar c b}{240} \left( \frac{1}{(g_0 - w)^4} - \frac{1}{(g_0 + w)^4} \right) \right\} \end{aligned} \quad (19)$$

Subject to the following boundary conditions:

$$w(0,t) = w(L,t) = 0, \quad \frac{\partial w(0,t)}{\partial x} = \frac{\partial w(L,t)}{\partial x} = 0 \quad (20)$$

where

$$(EI)_{eq} = EI + E^s I^s; \quad (EA)_{eq} = EA + E^s A^s; \quad (\rho A)_{eq} = \rho A + \rho^s A^s; \quad F_s = \tau_0 A^s + \tau_0 S_p \quad (21)$$

The integral term in Eq. (19) stands for midplane stretching of the nanobeam due to the immovable edges. For convenience, the following non-dimensional quantities are introduced:

$$\tilde{w} = \frac{w}{g_0}, \quad \tilde{x} = \frac{x}{L}, \quad \tilde{t} = \frac{t}{t^*}, \quad \tilde{\Omega} = \Omega t^* \quad (22)$$

where  $t^*$  is a characteristic time (timescale) defined as follows:

$$t^* = \sqrt{\frac{(\rho A)_{eq} L^4}{(EI)_{eq}}} \quad (23)$$

Substituting Eqs. (22) and (23) into Eq. (19) and dropping the tildes and assuming the AC voltage amplitude to be much less than the DC voltage ( $V_{AC}^2 \ll V_{DC}^2$ ), the non-dimensional form of the motion's equation by considering viscous damping ( $c_d$ ) and the corresponding boundary conditions are obtained:

$$\begin{aligned} (1 + \beta_3) \frac{\partial^4 w(x,t)}{\partial x^4} + \frac{\partial^2 w(x,t)}{\partial t^2} - (\beta_1 + \beta_2 \Gamma(w,w)) \frac{\partial^2 w(x,t)}{\partial x^2} + \beta_4 \frac{\partial w(x,t)}{\partial t} = \\ \beta_5 \left\{ \frac{1}{(1-w)^2} - \frac{1}{(1+w)^2} + b_0 \left( \frac{1}{1-w} - \frac{1}{1+w} \right) \right\} + 2\beta_5 R \cos(\Omega t) \left( \frac{1}{(1-w)^2} + \frac{b_0}{1-w} \right) + \\ \left\{ \beta_6 \left( \frac{1}{(1-w)^3} - \frac{1}{(1+w)^3} \right) \text{ or } \beta_7 \left( \frac{1}{(1-w)^4} - \frac{1}{(1+w)^4} \right) \right\} \end{aligned} \quad (24)$$

$$\begin{aligned} w(0,t) = w(1,t) = 0 \\ \frac{\partial w(0,t)}{\partial x} = \frac{\partial w(1,t)}{\partial x} = 0 \end{aligned} \quad (25)$$

The dimensionless parameters and the function  $\Gamma$  appearing in Eq. (24) are introduced as:

$$\begin{aligned} \Gamma(w_1(x,t), w_2(x,t)) = \int_0^1 \frac{\partial w_1}{\partial x} \cdot \frac{\partial w_2}{\partial x} dx \\ \beta_1 = \frac{F_s L^2}{(EI)_{eq}}, \quad \beta_2 = \frac{(EA)_{eq} g_0^2}{2(EI)_{eq}}, \quad \beta_3 = \frac{4\mu A l^2}{(EI)_{eq}}, \quad \beta_4 = \frac{c_d L^2}{\sqrt{(\rho A)_{eq} (EI)_{eq}}}, \quad \beta_5 = \frac{\varepsilon_0 b L^4 V_{DC}^2}{2g_0^3 (EI)_{eq}}, \\ \beta_6 = \frac{A_h b L^4}{6\pi g_0^4 (EI)_{eq}}, \quad \beta_7 = \frac{\pi^2 \hbar c b L^4}{240 g_0^5 (EI)_{eq}}, \quad b_0 = \frac{0.65}{b} g_0, \quad R = \frac{V_{AC}}{V_{DC}} \end{aligned} \quad (26)$$

## 2.4 Galerkin method

The partial differential equation of motion, Eq. (24), is converted to a set of ODEs through applying Galerkin's discretization method. The nanobeam deflection for reduced-order model (ROM) of the NEMS system can be written as the following finite series:

$$w(x;t) = \sum_{i=1}^N q_i(t) \varphi_i(x) \quad (27)$$

where  $N$  is the number of modes,  $\varphi_i$  is the  $i$ 'th eigenfunction of the clamped-clamped linear undamped nanobeam, incorporating the effect of surface energy, and  $q_i(t)$  indicates the time-dependent generalized coordinate



corresponding to the  $i$ 'th mode of vibration. It should be noted that,  $\varphi_i$  is normalized such that  $\int_0^1 \varphi_i \cdot \varphi_j dx = \delta_{ij}$  and satisfies the following eigenvalue problem:

$$\varphi_i^{IV} = \beta_1 \varphi_i'' + \omega_i^2 \varphi_i; \quad \varphi_i(x) = 0, \varphi_i'(x) = 0 \quad \text{at } x = 0, 1 \quad (28)$$

where  $\omega_i$  is the dimensionless natural frequency of the nanobeam. Substituting Eq. (27) into Eq. (24) and using Eq. (28) to eliminate  $\varphi_i^{IV}$ , then based on the Galerkin technique multiplying both sides by  $\varphi_n$ , and integrating the resultant over the length of the nanobeam reduces to

$$\begin{aligned} (1 + \beta_3) \left[ \beta_1 \sum_{i=1}^N K_{ni} q_i + \omega_n^2 q_n \right] + \ddot{q}_n - \left( \beta_1 + \beta_2 \int_0^1 \left( \sum_{i=1}^N q_i \varphi_i' \right)^2 dx \right) \sum_{i=1}^N K_{ni} q_i + \beta_4 \dot{q}_n = \\ \beta_5 \int_0^1 \varphi_n \cdot \left( \frac{1}{\left( 1 - \sum_{i=1}^N q_i \varphi_i \right)^2} - \frac{1}{\left( 1 + \sum_{i=1}^N q_i \varphi_i \right)^2} + b_0 \left( \frac{1}{1 - \sum_{i=1}^N q_i \varphi_i} - \frac{1}{1 + \sum_{i=1}^N q_i \varphi_i} \right) \right) dx + \\ 2\beta_5 R \cos(\Omega t) \int_0^1 \varphi_n \cdot \left( \frac{1}{\left( 1 - \sum_{i=1}^N q_i \varphi_i \right)^2} + \frac{b_0}{1 - \sum_{i=1}^N q_i \varphi_i} \right) dx + \left\{ \beta_6 \int_0^1 \varphi_n \cdot \left( \frac{1}{\left( 1 - \sum_{i=1}^N q_i \varphi_i \right)^3} - \frac{1}{\left( 1 + \sum_{i=1}^N q_i \varphi_i \right)^3} \right) dx \right. \quad \text{or} \quad (29) \\ \left. \beta_7 \int_0^1 \varphi_n \cdot \left( \frac{1}{\left( 1 - \sum_{i=1}^N q_i \varphi_i \right)^4} - \frac{1}{\left( 1 + \sum_{i=1}^N q_i \varphi_i \right)^4} \right) dx \right\}, \quad n = 1, 2, \dots, N \end{aligned}$$

where

$$K_{ni} = \int_0^1 \varphi_n(x) \cdot \varphi_i''(x) dx \quad (30)$$

Since Eq. (29) is too complex, it is almost impossible to present an analytical solution. Thus, the direct integration method is utilized which converts the  $n$  second-order differential equations of motion into  $2n$  first-order differential equations. Numerical integration is carried out based on Runge-Kutta method.

### 2.5 Approximated system

In this section, the condition for which the system is prone to exhibit chaotic behavior is obtained. In order to approximate the homoclinic trajectory of Eq. (24), it is common to extract the well-known Duffing-type equation along with its homoclinic orbit. To this end, all the autonomous terms on the right-hand side of Eq. (24) in a given time are expanded using Taylor series up to the fourth order; the resultant is:

$$\begin{aligned} (1 + \beta_3) \frac{\partial^4 w}{\partial x^4} + \frac{\partial^2 w}{\partial t^2} - (\beta_1 + \beta_2 \Gamma(w, w)) \frac{\partial^2 w}{\partial x^2} + \beta_4 \frac{\partial w}{\partial t} = \beta_5 (4w + 8w^3 + 2b_0(w + w^3)) + \\ \left\{ \beta_6 (6w + 20w^3) \text{ or } \beta_7 (8w + 40w^3) \right\} + O(w^5(x, t)) + 2\beta_5 R \cos(\Omega t) \left( \frac{1}{(1-w)^2} + \frac{b_0}{1-w} \right) \quad (31) \end{aligned}$$

As mentioned before, the value of the parameter  $R$  is much less than unity, and therefore the non-autonomous term on the right-hand side of Eq. (31) can be considered as a small perturbation to the remaining autonomous part of the system [13, 16, 56]. Implementing Galerkin discretization method for the single-DOF system and defining the following state space variables,

$$\begin{cases} S_1 \\ S_2 \end{cases} = \begin{cases} q_1 \\ \dot{q}_1 \end{cases} \quad (32)$$

The simplified model of the unperturbed system can be expressed as Eq. (33) through neglecting the harmonic excitation and damping effect.

$$\begin{aligned} \dot{S}_1 &= S_2 \\ \dot{S}_2 &= -K_l S_1 - K_n S_1^3 \end{aligned} \quad (33)$$

where  $K_l$  and  $K_n$ , respectively, denote the linear and cubic stiffness of the approximated system, and given by

$$\begin{aligned} K_l &= \omega_1^2 (1 + \beta_3) + \beta_1 \beta_3 K_1^n - 2\beta_5 (2 + b_0) - \{6\beta_6 \text{ or } 8\beta_7\} \\ K_n &= -\beta_2 K_1^n \Gamma(\varphi_1, \varphi_1) - 2\beta_5 K_2^n (4 + b_0) - 20K_2^n \{\beta_6 \text{ or } 2\beta_7\}, \quad K_2^n = \int_0^1 \varphi_1^4 dx \end{aligned} \quad (34)$$

The potential function of the unperturbed system which plays an important role in the definition of various dynamic behaviors of the nanobeam can be written as:

$$V(S_1) = K_l \frac{S_1^2}{2} + K_n \frac{S_1^4}{4} \quad (35)$$

The nanobeam dynamics can be classified into four classes according to the signs of the parameters  $K_l$  and  $K_n$ . Regarding this classification, four physical situations are addressed in Table 1. For case A, there exist only one unstable equilibrium point in the origin, thus any small perturbation causes the system trajectory gets far from the origin and finally leads to dynamic pull-in. For case B, there is only one center point at the origin, and a small perturbation leads to a closed trajectory surrounding the origin. The system motion corresponding to closed orbits are periodic and chaotic behavior does not occur in this case. For case C, there will be one stable center point in the origin and two unstable saddle nodes. Similar to case B, if the system is excited by a small perturbation, the system undergoes a closed trajectory surrounding the origin, with the difference that, the higher the actuation amplitude, the closer to the heteroclinic orbit the system trajectory gets. This results in intersecting the heteroclinic orbit which connects the two saddle points. Therefore, increasing the AC voltage amplitude may lead to the heteroclinic chaos in the response of the perturbed system. However, the results demonstrated that dynamic pull-in instability occurs immediately after the system response intersects the heteroclinic manifolds, and therefore, no chaotic motion is detected even for case C.

Consequently, chaos phenomenon is not observed in the response of the system for cases A to C. Finally, in case D, the system becomes bistable and contains three equilibrium points; one unstable saddle node at  $(0,0)$ , and two stable center points at  $(\pm\sqrt{-K_l/K_n}, 0)$ . For small values of AC voltage amplitude, the system undergoes a closed trajectory around one of the center points (depending on initial conditions). Increasing the actuation amplitude leads to intersection of the system trajectory and the homoclinic manifolds which result in homoclinic chaos.


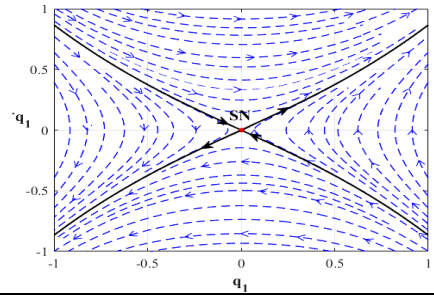

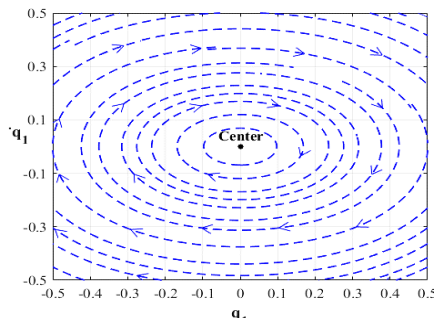

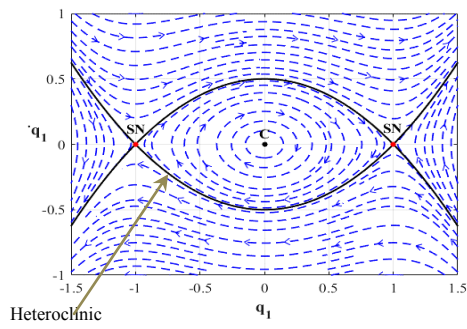
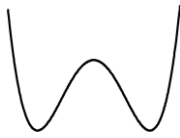
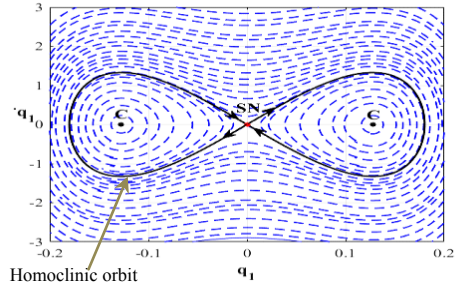
As shown in Table 1., the lower and upper bounds of  $\beta_3$  parameter,  $b_1$  and  $b_2$ , depend on non-dimensional size parameter ( $\beta_3$ ), surface parameter ( $\beta_1$ ) and intermolecular forces ( $\beta_6$  and  $\beta_7$ ). This means that, for a specified NEMS system with certain material and geometrical properties, definitely, the conditions of case D have been satisfied for DC voltage load ( $\beta_5$ ) if the system shows chaotic motion. It is worth mentioning that, if the influences of these parameters ( $\beta_1, \beta_3, \beta_6$  and  $\beta_7$ ) are considered to be neglected, the system's global behavior appears in another category for a certain value of the parameter  $\beta_5$ , since its corresponding lower and upper bounds vary.

Furthermore, it should be noted that, this approximation overestimates the DC load value resulting in chaos, and this can only be effective to gives the designer an initial estimation about the variation range of DC voltage load.

Generally speaking, including the effect of surface elasticity parameters in the system dynamics, and also classifying the nanoresonator's motion in to four categories based on DC voltage value can be considered as the most important achievements of the present work with respect to the study performed in Ref [39]. The main concentration of this work is to address chaotic motion taking place in the system response in the presence of all nanosized effects. For this purpose, bifurcation diagrams are proposed to capture the nature of the steady-state response of the system.

**Table 1**

Various categories based on the shape of potential function and corresponding phase portrait.

Case	Required condition	Potential function	Phase portrait
A	$\begin{cases} K_l \leq 0 \\ K_n \leq 0 \end{cases} \Rightarrow \beta_5 \geq \max(b_1, b_2)^*$		
B	$\begin{cases} K_l \geq 0 \\ K_n \geq 0 \end{cases} \Rightarrow \beta_5 \leq \min(b_1, b_2)$		
C	$\begin{cases} K_l > 0 \\ K_n < 0 \end{cases} \Rightarrow b_2 < \beta_5 < b_1$		
D	$\begin{cases} K_l < 0 \\ K_n > 0 \end{cases} \Rightarrow b_1 < \beta_5 < b_2$		

\*  $b_1 = (\omega_l^2(1 + \beta_3) + \beta_1\beta_3K_1^n - \{6\beta_6 \text{ or } 8\beta_7\})/2(2 + b_0)$  and  $b_2 = -(\beta_2K_1^n\Gamma(\varphi_1, \varphi_1) + 20K_2^n(\beta_6 \text{ or } 2\beta_7))/2K_2^n(4 + b_0)$

### 3 RESULTS AND DISCUSSION

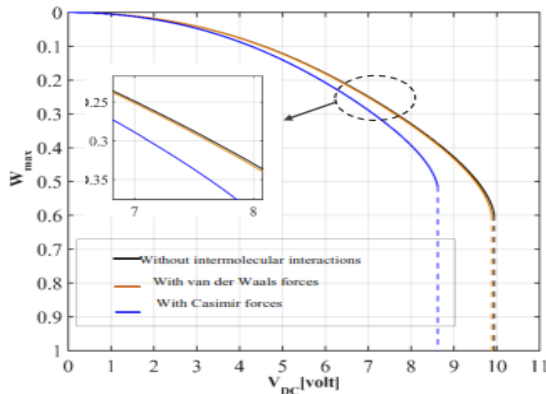
The nonlinear and chaotic behaviors of a silicon nanobeam are investigated for the case study. Geometrical parameters of the nanobeam, the values related to the mechanical properties of the bulk and surface layer are depicted in Table 2., (mechanical properties of the surface layer were adopted from [57]). According to [58, 59], it is common to consider size-dependent material parameter to be equal  $l = h/6$ . The non-dimensional damping coefficient  $\beta_4$  is set to be 0.1 throughout the simulations.

**Table 2**

Geometrical and material properties of the silicon nanobeam.

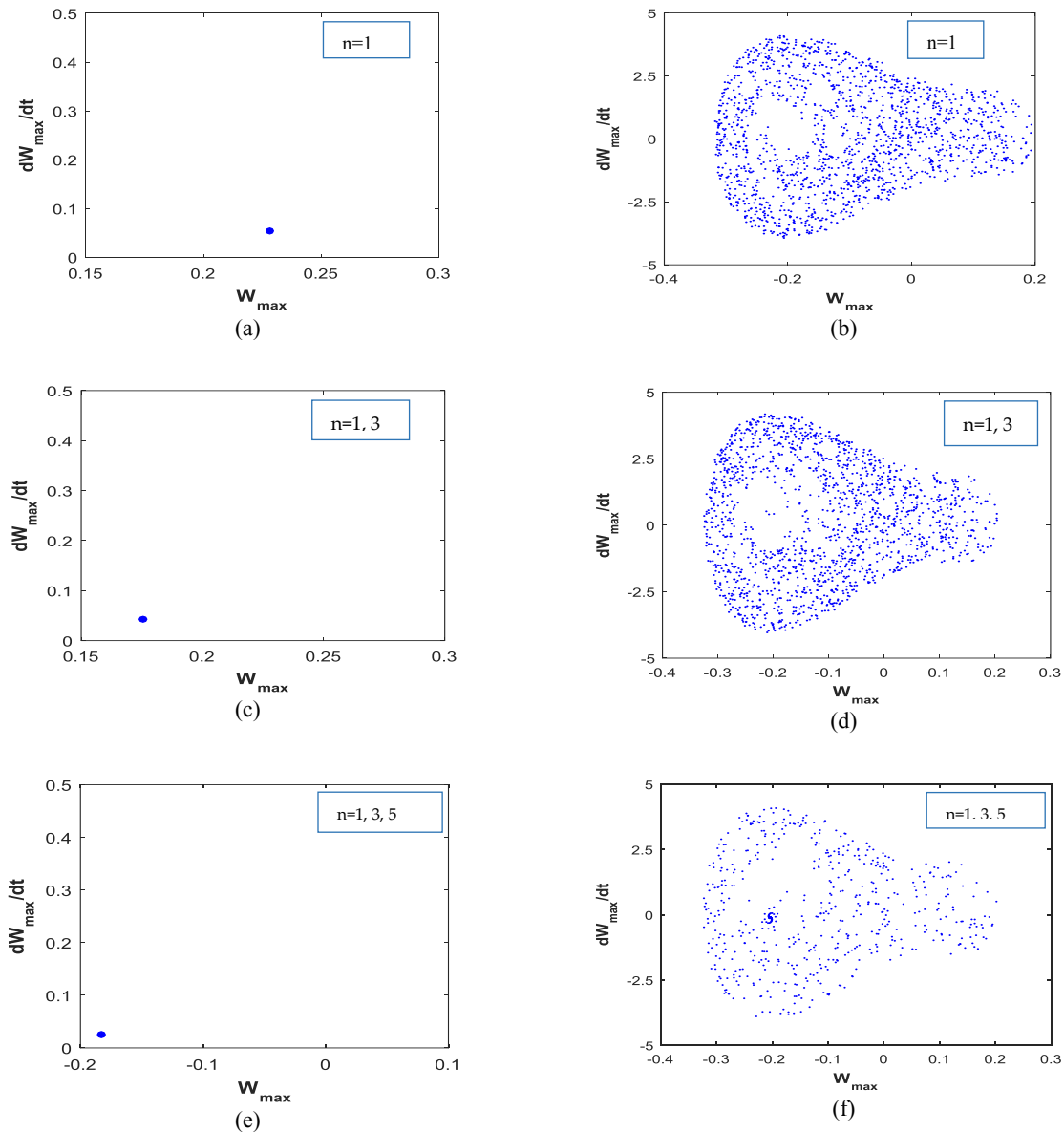
Parameters	Value
Length of the nanobeam, $L$	1000 nm
Width of the nanobeam, $b$	25 nm
Nanobeam thickness, $h$	10 nm
Young modulus, $E$	210 GPa
Mass density, $\rho$	2331 kg/m <sup>3</sup>
Poisson ratio, $\nu$	0.24
Initial gap, $g_0$	80 nm
Surface residual stress, $\tau_0$	0.605 N/m
Surface Young modulus, $E^s$	-10.036 N/m
Surface mass density, $\rho^s$	$3.17 \times 10^{-7}$ kg/m <sup>2</sup>

The influence of the interatomic forces on the midpoint static deflection of the nanobeam is illustrated in Fig. 2. It can be seen that, the van der Waals force effect slightly deviates the curve from that obtained in the absence of the dispersion forces; whereas both the amount of pull-in voltage and the static deflection are remarkably decreased while the effect of Casimir force is considered. In the rest part of the paper, the effect of Casimir regime is included in the dynamics of the nanobeam.



**Fig.2**  
Influence of the intermolecular interactions on the static deflection of the nanobeam midpoint.

The effect of number of modes of vibration on the steady-state motion of the system is illustrated in Fig. 3. Here, the symmetric eigenfunctions are only considered because of the symmetry in the configuration in the NEMS resonator and the electrostatic load. It is seen that, increasing the number of modes does not change the nature of the steady-state response (periodic or chaotic) of the system, but only estimates more accurately the amplitude of the states motion. In other words, the stability of the limit cycle is not affected by the number of vibration modes. Since the main contribution of the present work is to bifurcation analysis of the NEMS device considering the size and surface effects, single-mode approximation is sufficient to capture some ranges of the electrostatic load parameters in which the system exhibits periodic motion.

**Fig.3**

Influence of the number of modes on the system's steady-state behavior for  $\Omega = 5$ ,  $\beta_5 = 845$  and; (a), (c) and (e) for  $R=0.001$ ; (b), (d) and (f) for  $R=0.005$ .

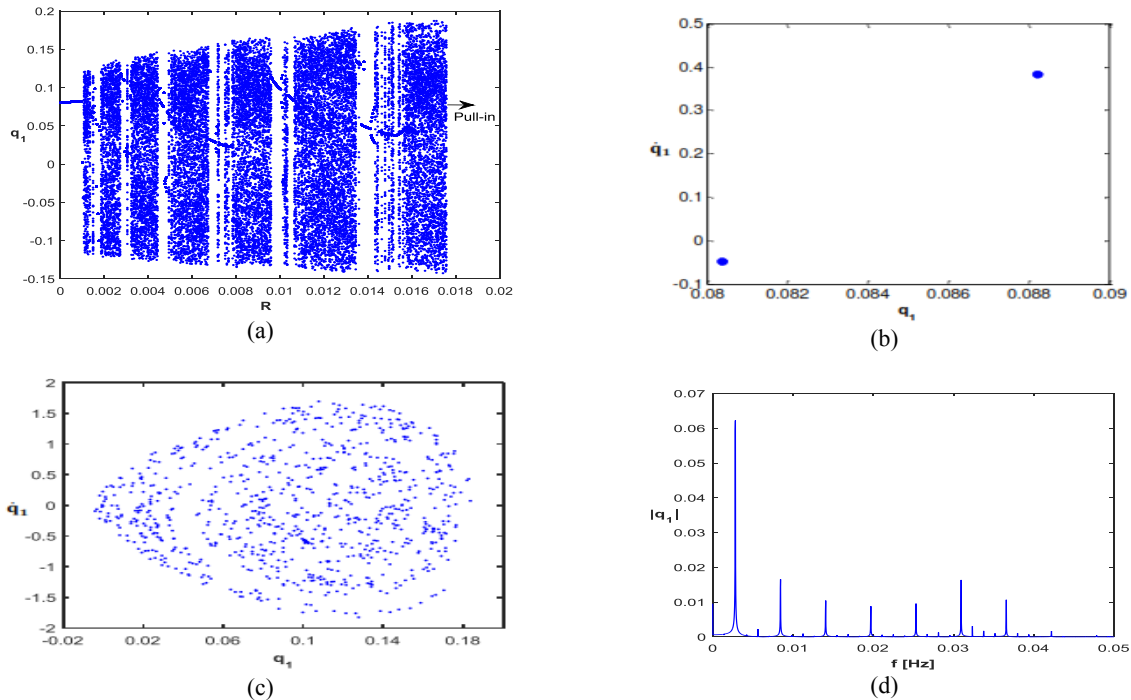
### 3.1 Bifurcation and chaos

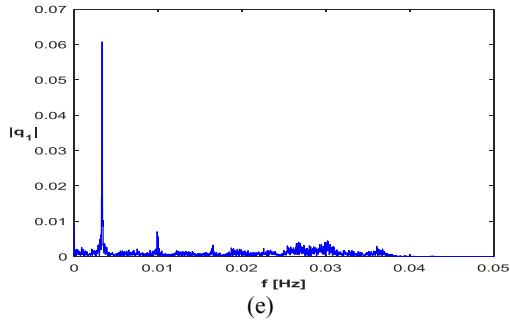
In general, nano-electro-mechanical systems with double-sided electrostatic actuation are well-known to exhibit chaotic motion. Sensitivity-dependence on initial conditions and external load parameters are the main characteristics of the NEMS devices resulting in periodic behaviors in some values of DC and AC voltages' amplitude. Therefore, it is very important to evaluate a range of these parameters, which result in a stable periodic orbit after the steady state response of the system reaches. In the following, the continuous-time dynamics of the system is converted to discrete-time domain using Poincaré portrait. The periodicity of the orbit is exactly reflected in the Poincaré portrait. Since the continuous-time trajectory undergoes periodic motion, for the case of stable fixed point, there exist a finite number of points on the Poincaré portrait, equal to the periodicity of the limit cycle. The system behavior is said to be quasi-periodic when a closed curve is appears on the map. For a chaotic dynamic behavior, the orbit is nonperiodic and bounded, and there are innumerable points on the Poincaré portrait, included

within a finite zone and spread over a region of very complex structure. FFT analysis is carried out in order to exploit the frequency content of the system response. Chaos phenomenon is detected while there is a wide output frequency spectrum for the system input of harmonic motion with single frequency. In this case, a wide range of frequencies along with disturbances are visible in FFT plots. For the case of periodic motion, there are differentiable high peaks at the system natural frequency and its harmonics. In the following, actuation amplitude and DC voltage amplitude are synonyms to the  $R$  and  $\beta_5$  non-dimensional parameters, respectively, and system response defines the  $q_1$  motion.

In order to analyze the global dynamics of the NEMS system, bifurcation diagrams are extracted. For this purpose, the system states are mapped at equal intervals once every  $T$  seconds for a specified value of actuation amplitude, where  $T$  is the period of the external harmonic excitation. This process is applied during numerical simulation of the motion equation for a time interval of  $[0, 2500]$  dimensionless seconds. The first 70% of the results were removed to exclude possible transient vibrations from the calculated Poincaré portrait. Then, the remaining points in this section representing the steady-state behavior of the system in the discrete Poincaré portrait are plotted versus the actuation amplitude. In the present work, this process is repeated for 500 values of actuation amplitude. Matlab code is utilized to perform the numerical computations. Simulation runtime for extracting each bifurcation diagram takes about 10 h in a PC with 3.5 GHz processor and 8.0 GB RAM.

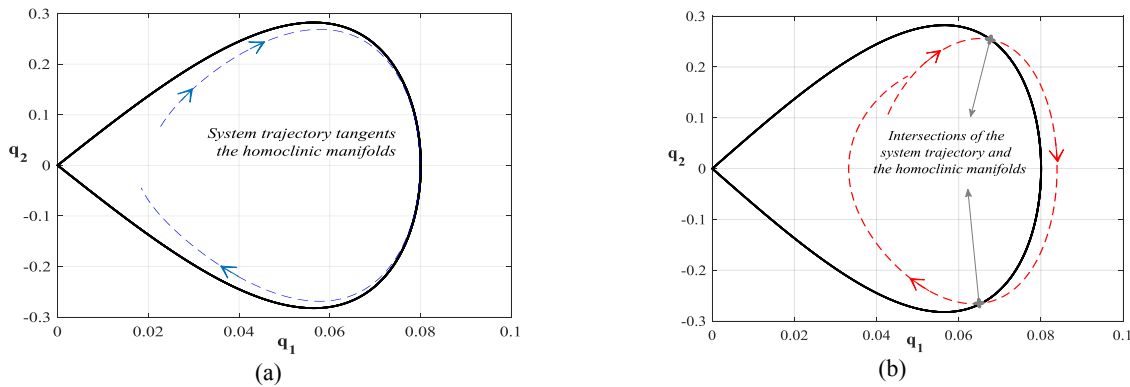
In this section, a comprehensive study is conducted on bifurcation analysis with varying actuation amplitude corresponding to different values of applied DC voltage. The effect of excitation frequency on the system response is also investigated. Fig. 4 illustrates the bifurcation diagram, Poincaré portraits and FFT plots for an excitation frequency of  $\Omega = 2$  and DC voltage amplitude of  $\beta_5 = 830$ . As observed in this figure, there are many white bands of different widths among the smudge of dots showing the occurrence of chaos. These are periodic windows, where the system comes out of chaos. At first, the system exhibits period-one motion and continues up to the actuation amplitude of  $R=0.0011$ . Further increase in the parameter causes abrupt change in the system response so that the chaotic regime begins with no branching manner. This is known as dangerous bifurcation which is widely appeared in dynamic analysis of the NEMS. Then, the amplitude of the system response increases proportional to the forcing amplitude, and eventually the nanobeam collapses at  $R=0.0176$ . It is observed that chaotic behavior is dominant in the whole range of the parameter. In the case of chaotic motion, frequency response of the system contains disturbances between two successive high peaks. For period-two motion, the distance between two recognizable peaks is equal to one half of the system fundamental frequency and the plot is smooth in other frequencies (Fig. 4(e), d).





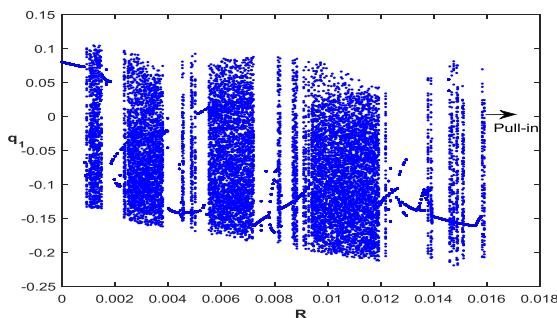
**Fig.4**  
 Dynamic response of the system for  $\Omega = 2$  and  $\beta_5 = 830$ ; (a) Bifurcation diagram with varying actuation amplitude, (b) Poincaré portrait and (d) FFT plot for  $R=0.0142$ , (c) Poincaré portrait and (e) FFT plot for  $R=0.008$ .

A partial of the system path for two different values of bifurcation parameter corresponding to Fig. 4 has been drawn in Fig. 5. As illustrated in Fig. 5(a), the trajectory of the system tangents to the homoclinic manifolds while the actuation amplitude is set to 0.001, and a slight increment in the bifurcation parameter results in intersection between the system solution and the homoclinic branches, bring the system into chaotic regime. At this point, the limit cycle is marginally stable and saddle-node bifurcation takes place while the parameter is further increased. As expected, the system trajectory intersects the homoclinic manifolds for  $R=0.0015$  since it is a candidate of chaotic response, Fig. 5(b).



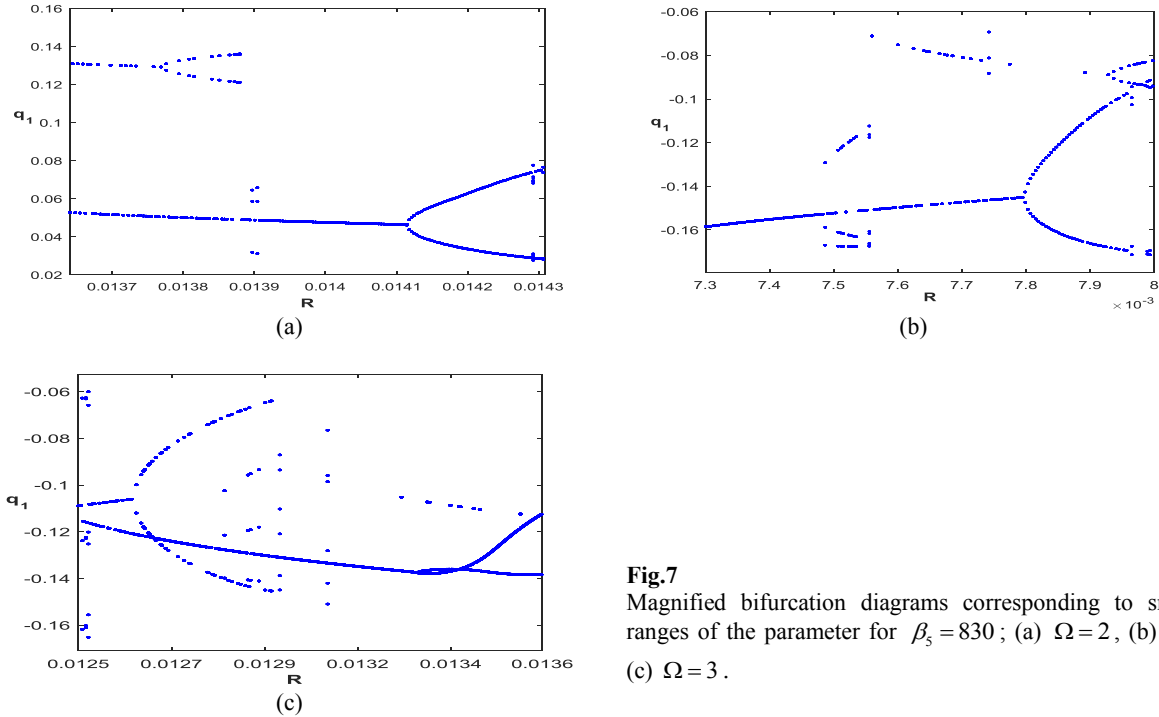
**Fig.5**  
 Dynamic response of the system for  $\Omega = 2$  and  $\beta_5 = 830$ ; (a) The system trajectory tangents the homoclinic manifolds for  $R=0.001$ ; (b) The system trajectory intersects the homoclinic orbit for  $R=0.0015$ .

Fig. 6 indicates the bifurcation diagram for the excitation frequency of  $\Omega = 3$ . As shown in this figure, the width of the periodic windows becomes larger when the excitation frequency increases. The system behavior is commenced by period-one as previous, and it is continuous up to the actuation amplitude 0.0008. As observed, the limit cycle is unstable just before dynamic pull-in. Finally, dynamic pull-in instability occurs when the actuation amplitude reaches critical value 0.0159. According to Fig. 6, it can be concluded that the system response tends to be dominantly periodic at larger values of actuation amplitude, and dynamic pull-in threshold decreases when the excitation load frequency increases. Furthermore, jumps phenomenon between two periodic orbits is detected in the system response at some value of the parameter.



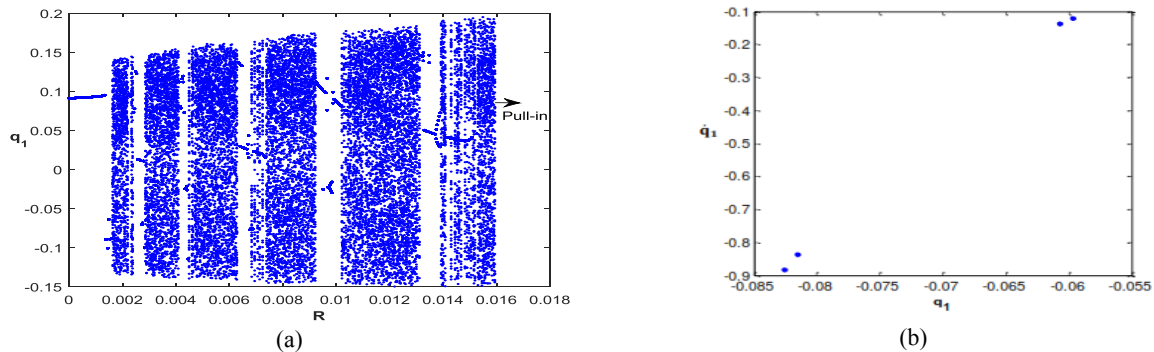
**Fig.6**  
 Bifurcation diagram with varying actuation amplitude for  $\Omega = 3$  and  $\beta_5 = 830$ .

In Fig. 7, one stable region in the interval [0.0136, 0.0143] for  $\Omega=2$ , and two stable regions in the intervals [0.0073, 0.008] and [0.0125, 0.0136] for  $\Omega=3$  are magnified to obtain more detailed bifurcations in the system response. According to Fig. 7(a), in the actuation amplitude range of [0.0136, 0.0138], the motion of the system is periodic so that it jumps between two coexisting period-one attractors several times. Period-doubling bifurcation occurs in both the upper and lower solution branches. As observed in Figs. 7(b) and 7(c), the system behavior is commenced by period-one motion, and in some ranges of the parameter, there exist higher periodic orbits such as, period-3 and period-6 limit cycles.

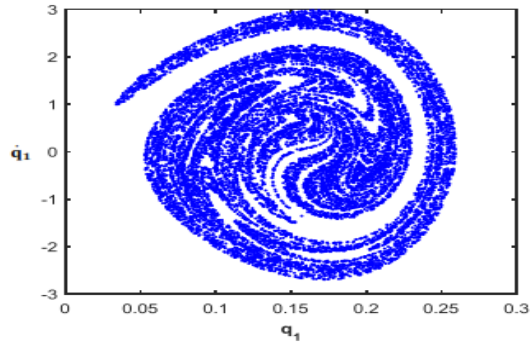


**Fig.7** Magnified bifurcation diagrams corresponding to small ranges of the parameter for  $\beta_5 = 830$ ; (a)  $\Omega=2$ , (b) and (c)  $\Omega=3$ .

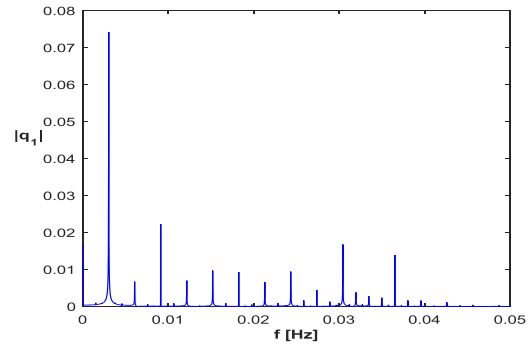
Figs. 8 and 9 demonstrate the bifurcation diagrams, Poincaré portraits and FFT plots for an excitation frequency of  $\Omega=2$ , and DC voltage amplitudes of  $\beta_5 = 835$  and  $\beta_5 = 858$ , respectively. According to the figure, the generic behavior of the NEMS is similar to the previous case for  $\beta_5 = 830$ , but the initial stable region of the system response is increased. Increasing the value of DC voltage amplitude results in decreasing the number of periodic windows as well as dynamic pull-in threshold. As depicted in Fig. 9, for low values of the actuation amplitude, the saddle-node bifurcation occurs in a wider range of the parameter. Because the desired NEMS is a high-order nonlinear system, more complex, Poincaré portraits are expected. Strange attractor with extremely complex geometry is observed for this high dimension nonlinear system, inferring that chaos and fractal phenomena exist in the response of the system. Fractal means that the geometry has infinite details and self-similar structures at different levels of magnification [60, 61].



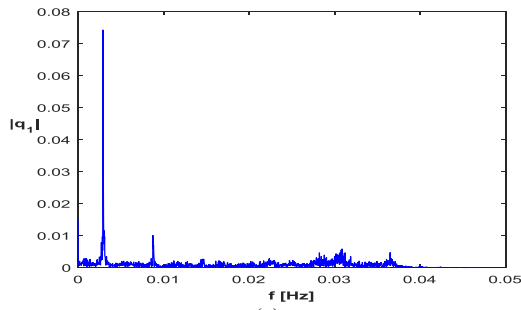




(c)



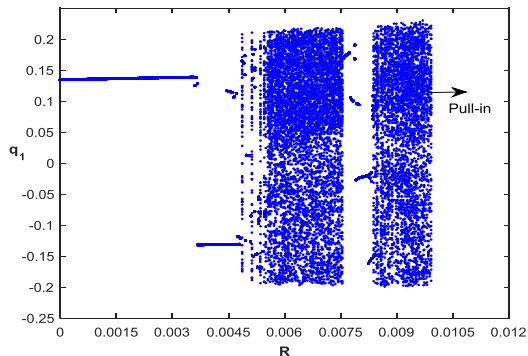
(d)



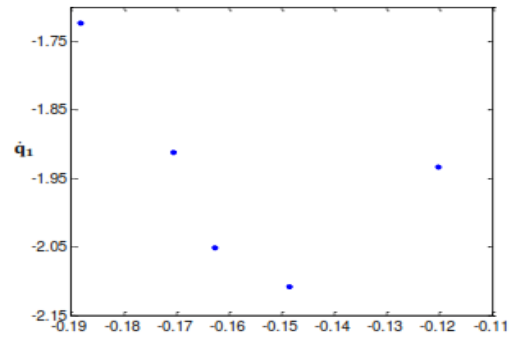
(e)

**Fig.8**

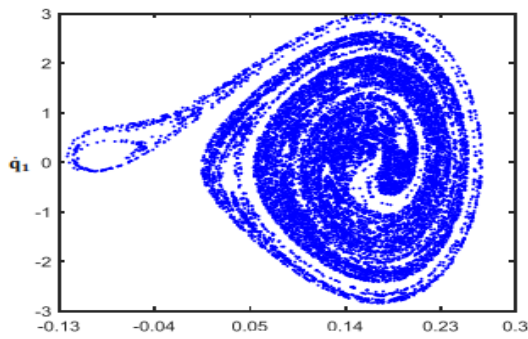
Dynamic response of the system for  $\Omega=2$  and  $\beta_s=835$  ;  
 (a) Bifurcation diagram with varying actuation amplitude,  
 (b) Poincaré portrait and (d) FFT plot for  $R=0.0097$ , (c)  
 Poincaré portrait and (e) FFT plot for  $R=0.0125$ .



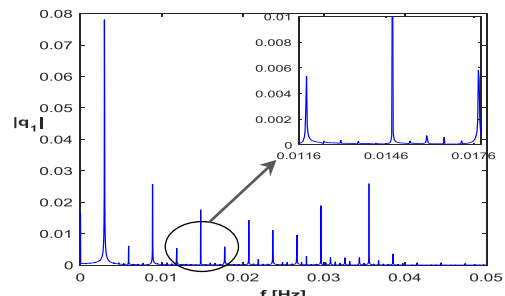
(a)



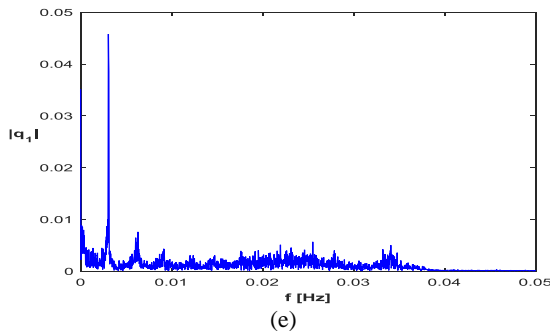
(b)



(c)



(d)

**Fig.9**

Dynamic response of the system for  $\Omega=2$  and  $\beta_s=858$  ;  
 (a) Bifurcation diagram with varying actuation amplitude,  
 (b) Poincaré portrait and (d) FFT plot for  $R=0.00798$ , (c)  
 Poincaré portrait and (e) FFT plot for  $R=0.006$ .

#### 4 CONCLUSIONS

In this paper, the chaotic behavior of a nanobeam actuator with double-sided electrostatic actuation was investigated. In order to consider the influence of small-scale in the NEMS device, consistent couple stress theory proposed by Hadjesfandiari and Dargush is utilized. The surface energy effect as well as intermolecular interactions are included in the mathematical model of the system. Motion differential equation was established based on Hamilton's principle and discretized to a set of nonlinear ODEs through Galerkin's procedure. Numerical integration method was used to solve the dynamic equation, and the analysis of static pull-in voltage was performed to validate the proposed formulation.

The DC and AC voltages' amplitude and the excitation frequency are three parameters, which significantly influence the dynamic response of the NEMS system. A nanobeam made of silicon was used as a case study to perform the nonlinear analysis. Poincaré portrait and FFT analysis were applied to represent the system behavior in discrete state-space and frequency domain, respectively. These are known as convenient tools to identify the system dynamic behavior, especially chaos. For this nonlinear system, strange attractors and chaos phenomenon were observed. Bifurcation analysis with varying actuation amplitude is carried out for different values of DC voltage amplitude and excitation frequency. For low values of these parameters, the NEMS predominantly exhibits chaotic motion in the whole range of actuation amplitude. Some ranges of the forcing amplitude were presented in which the embedded periodic orbit of the system response becomes stable. From Figs. 4, 6, 8, and 9, it can be concluded that there is an initial stable region in which the system's trajectory contains period-one orbit. Therefore, when the DC voltage amplitude increases, the interval contains a wider range of actuation amplitude. Increasing either the excitation frequency or the DC voltage amplitude causes that the system becomes dynamically unstable at smaller values of the actuation parameter, as expected. According to the findings of the study, an increase in value of excitation frequency does not always result in lengthening the initial periodic interval, in which the system's trajectory has a stable period-one orbit. The presented results can be used in controlling novel NEMS devices. In the future works, feedback linearization method will be utilized in order to suppress the chaotic motion appeared in some ranges of the electrostatic load parameters. The analysis performed in this paper can be useful for detecting the electrostatic load parameters in which the system limit cycle becomes unstable, and therefore one can apply appropriate control method in order to eliminate chaos. The obtained results in this manuscript help the designer to find the correct regions in which the NEMS system is prone to chaotic motion. Furthermore, some points at which sudden changes in the system behavior take place were examined. This can help the engineer designers to tune the system parameters so that the NEMS device operates far from this dangerous bifurcation points.

#### REFERENCES

- [1] Mayoof F. N., Hawwa M. A., 2009, Chaotic behavior of a curved carbon nanotube under harmonic excitation, *Chaos, Solitons & Fractals* **42**(3):1860-1867.
- [2] Amorim T. D., Dantas W. G., Gusso A., 2015, Analysis of the chaotic regime of MEMS/NEMS fixed-fixed beam resonators using an improved 1DOF model, *Nonlinear Dynamics* **79**(2): 967-981.
- [3] Sabarathinam S., Thamilmaran K., 2016, Implementation of analog circuit and study of chaotic dynamics in a generalized Duffing-type MEMS resonator, *Nonlinear Dynamics* **2016**:1-12.
- [4] Hu W., Song M., Deng Z., Zou H., Wei B., 2017, Chaotic region of elastically restrained single-walled carbon nanotube, *Chaos: An Interdisciplinary Journal of Nonlinear Science* **27**(2): 023118.

- [5] Bienstman J., Vandewalle J., Puers R., 1998, The autonomous impact resonator: a new operating principle for a silicon resonant strain gauge, *Sensors and Actuators A: Physical* **66**(1): 40-49.
- [6] Luo A. C., Wang F.-Y., 2002, Chaotic motion in a micro-electro-mechanical system with non-linearity from capacitors, *Communications in Nonlinear Science and Numerical Simulation* **7**(1): 31-49.
- [7] Luo A. C., Wang F.-Y., 2004, Nonlinear dynamics of a micro-electro-mechanical system with time-varying capacitors, *Journal of Vibration and Acoustics* **126**(1): 77-83.
- [8] DeMartini B. E., Butterfield H. E., Moehlis J., Turner K. L., 2007, Chaos for a microelectromechanical oscillator governed by the nonlinear Mathieu equation, *Journal of Microelectromechanical Systems* **16**(6): 1314-1323.
- [9] Wang Y. C., Adams S. G., Thorp J. S., MacDonald N. C., Hartwell P., Bertsch F., 1998, Chaos in MEMS, parameter estimation and its potential application, *IEEE Transactions on Circuits and Systems, Fundamental Theory and Applications* **45**(10): 1013-1020.
- [10] Zhang W.-M., Tabata O., Tsuchiya T., Meng G., 2011, Noise-induced chaos in the electrostatically actuated MEMS resonators, *Physics Letters A* **375**(32): 2903-2910.
- [11] Aghababa M. P., 2012, Chaos in a fractional-order micro-electro-mechanical resonator and its suppression, *Chinese Physics B* **21**(10): 100505.
- [12] Li H., Liao X., Ullah S., Xiao L., 2012, Analytical proof on the existence of chaos in a generalized Duffing-type oscillator with fractional-order deflection, *Nonlinear Analysis: Real World Applications* **13**(6): 2724-2733.
- [13] Miandoab E. M., Yousefi-Koma A., Pishkenari H. N., Tajaddodianfar F., 2015, Study of nonlinear dynamics and chaos in MEMS/NEMS resonators, *Communications in Nonlinear Science and Numerical Simulation* **22**(1): 611-622.
- [14] Seleim A., Towfighian S., Delande E., Abdel-Rahman E., Heppler G., 2012, Dynamics of a close-loop controlled MEMS resonator, *Nonlinear Dynamics* **69**(1-2): 615-633.
- [15] Han J., Zhang Q., Wang W., 2015, Design considerations on large amplitude vibration of a doubly clamped microresonator with two symmetrically located electrodes, *Communications in Nonlinear Science and Numerical Simulation* **22**(1): 492-510.
- [16] Haghighi H. S., Markazi A. H., 2010, Chaos prediction and control in MEMS resonators, *Communications in Nonlinear Science and Numerical Simulation* **15**(10): 3091-3099.
- [17] Yau H.-T., Wang C.-C., Hsieh C.-T., Cho C.-C., 2011, Nonlinear analysis and control of the uncertain micro-electro-mechanical system by using a fuzzy sliding mode control design, *Computers & Mathematics with Applications* **61**(8): 1912-1916.
- [18] Zhankui S., Sun K., 2013, Nonlinear and chaos control of a micro-electro-mechanical system by using second-order fast terminal sliding mode control, *Communications in Nonlinear Science and Numerical Simulation* **18**(9): 2540-2548.
- [19] Tusset A., Balthazar J. M., Bassinello D., Pontes Jr B., Felix J. L. P., 2012, Statements on chaos control designs, including a fractional order dynamical system, applied to a "MEMS" comb-drive actuator, *Nonlinear Dynamics* **69**(4): 1837-1857.
- [20] Tusset A. M., Bueno A. M., Nascimento C. B., dos Santos Kaster M., Balthazar J. M., 2013, Nonlinear state estimation and control for chaos suppression in MEMS resonator, *Shock and Vibration* **20**(4): 749-761.
- [21] Tajaddodianfar F., Hairri Yazdi M. R., Pishkenari H. N., 2015, On the chaotic vibrations of electrostatically actuated arch micro/nano resonators: a parametric study, *International Journal of Bifurcation and Chaos* **25**(08): 1550106.
- [22] Ni X., Ying L., Lai Y.-C., Do Y., Grebogi C., 2013, Complex dynamics in nanosystems, *Physical Review E* **87**(5): 052911.
- [23] Hu W., Deng Z., Wang B., Ouyang H., 2013, Chaos in an embedded single-walled carbon nanotube, *Nonlinear Dynamics* **72**(1-2): 389-398.
- [24] Coluci V., Legoas S., de Aguiar M., Galvao D., 2005, Chaotic signature in the motion of coupled carbon nanotube oscillators, *Nanotechnology* **16**(4): 583.
- [25] Hawwa M., Mayoof F., 2009, Nonlinear oscillations of a carbon nanotube resonator, *International Symposium on Mechatronics and its Applications*, Sharjah.
- [26] Hawwa M. A., Al-Qahtani H. M., 2010, Nonlinear oscillations of a double-walled carbon nanotube, *Computational Materials Science* **48**(1): 140-143.
- [27] Joshi A. Y., Sharma S. C., Harsha S., 2012, Chaotic response analysis of single-walled carbon nanotube due to surface deviations, *Nanotechnology* **7**(02): 1250008.
- [28] Ashhab M., Salapaka M., Dahleh M., Mezić I., 1999, Melnikov-based dynamical analysis of microcantilevers in scanning probe microscopy, *Nonlinear Dynamics* **20**(3): 197-220.
- [29] Ashhab M., Salapaka M. V., Dahleh M., Mezić I., 1999, Dynamical analysis and control of microcantilevers, *Automatica* **35**(10): 1663-1670.
- [30] Basso M., Giarre L., Dahleh M., Mezić I., 1998, Numerical analysis of complex dynamics in atomic force microscopes, *Proceedings of the 1998 IEEE International Conference* **2**: 1026-1030.
- [31] Balthazar J. M., Tusset A. M., Bueno A., 2014, TM-AFM nonlinear motion control with robustness analysis to parametric errors in the control signal determination, *Journal of Theoretical and Applied Mechanics* **52**: 93-106.
- [32] Jamitzky F., Stark M., Bunk W., Heckl W., Stark R., 2006, Chaos in dynamic atomic force microscopy, *Nanotechnology* **17**(7): S213.
- [33] Raman A., Hu S., 2006, Chaos in dynamic atomic force microscopy, *International Symposium on Nonlinear Theory and Its Applications*, Bologna, Italy.

- [34] Lin W.-H., Zhao Y.-P., 2005, Nonlinear behavior for nanoscale electrostatic actuators with Casimir force, *Chaos, Solitons & Fractals* **23**(5): 1777-1785.
- [35] Abdel-Rahman E. M., Nayfeh A. H., 2003, Secondary resonances of electrically actuated resonant microsensors, *Journal of Micromechanics and Microengineering* **13**(3): 491.
- [36] Ouakad H. M., Younis M. I., 2010, Nonlinear dynamics of electrically actuated carbon nanotube resonators, *Journal of Computational and Nonlinear Dynamics* **5**(1): 011009.
- [37] Nayfeh A. H., Balachandran B., 1995, *Applied Nonlinear Dynamics: Analytical, Computational, and Experimental Methods*, Wiley Series in Nonlinear Sciences, John Wiley & Sons, Inc New York.
- [38] Younis M. I., 2011, *MEMS Linear and Nonlinear Statics and Dynamics*, Springer Science & Business Media.
- [39] Kivi A. R., Azizi S., Norouzi P., 2017, Bifurcation analysis of an electrostatically actuated nano-beam based on modified couple stress theory, *Sensing and Imaging* **18**(1): 32.
- [40] Chen X., Meguid S., 2017, Dynamic behavior of micro-resonator under alternating current voltage, *International Journal of Mechanics and Materials in Design* **13**: 481-497.
- [41] Nikpourian A., Ghazavi M. R., Azizi S., 2018, On the nonlinear dynamics of a piezoelectrically tuned micro-resonator based on non-classical elasticity theories, *International Journal of Mechanics and Materials in Design* **14**: 1-19.
- [42] Pourkiaee S. M., Khadem S. E., Shahgholi M., 2016, Parametric resonances of an electrically actuated piezoelectric nanobeam resonator considering surface effects and intermolecular interactions, *Nonlinear Dynamics* **84**: 1943-1960.
- [43] Hajnayeb A., Khadem S., 2011, Nonlinear vibrations of a carbon nanotube resonator under electrical and van der Waals forces, *Journal of Computational and Theoretical Nanoscience* **8**(8): 1527-1534.
- [44] Hajnayeb A., Khadem S., 2012, Nonlinear vibration and stability analysis of a double-walled carbon nanotube under electrostatic actuation, *Journal of Sound and Vibration* **331**(10): 2443-2456.
- [45] Batra R. C., Porfiri M., Spinello D., 2008, Effects of van der Waals force and thermal stresses on pull-in instability of clamped rectangular microplates, *Sensors* **8**(2): 1048-1069.
- [46] Lamoreaux S. K., 2004, The Casimir force: background, experiments, and applications, *Reports on Progress in Physics* **68**(1): 201.
- [47] Gupta R. K., 1998, Electrostatic pull-in test structure design for in-situ mechanical property measurements of microelectromechanical systems (MEMS), *Thesis Ph. D. Massachusetts Institute of Technology, Department of Electrical Engineering and Computer Science*.
- [48] Huang J.-M., Liew K., Wong C., Rajendran S., Tan M., Liu A., 2001, Mechanical design and optimization of capacitive micromachined switch, *Sensors and Actuators A: Physical* **93**(3): 273-285.
- [49] Mindlin R., Tiersten H., 1962, Effects of couple-stresses in linear elasticity, *Archive for Rational Mechanics and Analysis* **11**(1): 415-448.
- [50] Stölken J., Evans A., 1998, A microbend test method for measuring the plasticity length scale, *Acta Materialia* **46**(14): 5109-5115.
- [51] Hadesfandiari A. R., Dargush G. F., 2011, Couple stress theory for solids, *International Journal of Solids and Structures* **48**(18): 2496-2510.
- [52] Osterberg P. M., Senturia S. D., 1997, M-TEST: a test chip for MEMS material property measurement using electrostatically actuated test structures, *Journal of Microelectromechanical Systems* **6**(2): 107-118.
- [53] Gurtin M. E., Murdoch A. I., 1975, A continuum theory of elastic material surfaces, *Archive for Rational Mechanics and Analysis* **57**(4): 291-323.
- [54] Gurtin M. E., Murdoch A. I., 1978, Surface stress in solids, *International Journal of Solids and Structures* **14**(6): 431-440.
- [55] Ru C., 2010, Simple geometrical explanation of Gurtin-Murdoch model of surface elasticity with clarification of its related versions, *Science China Physics, Mechanics and Astronomy* **53**(3): 536-544.
- [56] Azizi S., Ghazavi M.-R., Khadem S. E., Rezazadeh G., Cetinkaya C., 2013, Application of piezoelectric actuation to regularize the chaotic response of an electrostatically actuated micro-beam, *Nonlinear Dynamics* **73**(1-2): 853-867.
- [57] Zhu R., Pan E., Chung P. W., Cai X., Liew K. M., Buldum A., 2006, Atomistic calculation of elastic moduli in strained silicon, *Semiconductor Science and Technology* **21**(7): 906.
- [58] Akgöz B., Civalek Ö., 2011, Strain gradient elasticity and modified couple stress models for buckling analysis of axially loaded micro-scaled beams, *International Journal of Engineering Science* **49**(11): 1268-1280.
- [59] Alemansour H., Miandoab E. M., Pishkenari H. N., 2017, Effect of size on the chaotic behavior of nano resonators, *Communications in Nonlinear Science and Numerical Simulation* **44**: 495-505.
- [60] Chen Y., 1993, *Bifurcation and Chaos Theory of Nonlinear Vibration Systems*, Higher Education, Beijing, China.
- [61] Guckenheimer J., Holmes P. J., 2013, *Nonlinear Oscillations, Dynamical Systems, and Bifurcations of Vector Fields*, Springer Science & Business Media.